Progress In Electromagnetics Research B, Vol. 112, 43–59, 2025

*(Received 16 April 2025, Accepted 16 May 2025, Scheduled 31 May 2025)*

# Multi-Physics Coupling Analysis of Vibration and Noise Abnormalities in Transformer under Geomagnetically Induced Current

Chao Pan, Chuanhui Wang*, Tongrui Fu, and Shoukun Zou

*Key Laboratory of Modern Power System Simulation and Control & Renewable Energy Technology Ministry of Education (Northeast Electric Power University), Jilin 132012, China*

**ABSTRACT:** Focusing on the instability problems of power grid transformer caused by geomagnetically induced current (GIC), this paper investigates the multi-physics coupling characteristics of a transformer under GIC. First, the propagation path of GIC is analyzed, and the variation characteristics are further studied based on measurement data. The variational signatures can be characterized by two key parameters: GIC distortion rate ($\Delta k$) and distortion time ($t_\tau$). A multi-physics coupling model considering GIC distortion is proposed, which includes mechanical domain coupling between electromagnetic and acoustic domains. Simulations are conducted on a three-phase transformer under varying conditions of $\Delta k$, $t_\tau$, and load factor ($\eta$). Then, the spatial-temporal variations of winding current, magnetic leakage, core vibration acceleration, and noise can be analyzed. Results reveal that vibration and noise exhibit abnormal intensification under GIC interference. Meanwhile, dynamic experimental platform is established. And the result is verified through consistency of virtual model and physical entity. On this basis, a nonlinear mapping relationship between $\Delta k$ and sound pressure level ($L_p$) is established. Finally, a stability criterion is developed to represent anomalies in terms of thresholds, providing a foundation for situational awareness and full lifecycle management of grid equipment under GIC interference.

## 1. INTRODUCTION

During intense solar storms or geomagnetic disturbances, significant variations in planetary magnetosphere and ionosphere can induce substantial geomagnetically induced current (GIC). Transformers can be disturbed by GIC through grounding points, which poses critical challenges to power transmission networks due to its long duration and extensive spatial propagation [1, 2]. Recently, worldwide power grid problems caused by GIC have become increasingly prominent [3, 4].

Excitation saturation, distorted current, and harmonic distortion are induced in transformer when being affected by GIC. Meanwhile, these situations are accompanied by abnormalities such as loss increase, vibration intensification and noise anomalies. In [5], harmonic distortion components of the transformer under GIC interference are investigated, which reveals that 100 Hz harmonics exhibit the highest proportion. Ref. [6] concludes that elevated levels of GIC induce significant stray losses by utilizing a topological transformer model and three-dimensional finite element analysis. In [7], GIC is approximately equivalent to direct current (DC) interference. By leveraging the Extended Kalman Filter, a new method for real-time prediction of GIC is proposed. Ref. [8] systematically investigates the intrinsic relationship between GIC and reactive power losses through a single-phase transformer. A comparative analysis on current harmonic distortion in transformer primary and secondary winding is carried out in [9], under different degrees of GIC. A low-frequency transient model is proposed in [10] to characterize the magnetic flux and thermal distributions within cores and tanks under GIC interference. A feature vector is developed in [11], which can be used to determine transformer vibration level under DC bias interference. By taking a three-phase transformer under DC bias as an example, the vibration characteristic is analyzed in [12]. Through field experiments, the impact of DC bias effects on the core magnetostriction characteristics is studied in [13].

In summary, due to the low-frequency characteristic of GIC, existing studies approximate it as DC to analyze the impact on transformer. In [14], a saturable transformer unified magnetic equivalent (UMEC) model is proposed to study the impact of GIC on saturation. In [15], the B-H magnetization curve is used to characterize the nonlinear characteristics of transformer core, and it is demonstrated that five-limb transformers are more susceptible to GIC. However, the correlation between time-domain fluctuation of GIC and vibration-induced noise of transformer is rarely studied in depth.

In [16], aiming to investigate the characteristics of transformer under three-phase load unbalance, a coupled electromagnetic, conjugate heat transfer, and mechanical multi-physics model is developed. In [17], a stress and electromagnetic coupling model is built to obtain the vibration characteristics of oil-immersed transformer winding. Compared with the above literature, a multi-physics coupling model which includes the coupling of electromagnetic, mechanical

---

* Corresponding author: Chuanhui Wang (1249593929@qq.com).

doi:10.2528/PIERB25041605

Published by THE ELECTROMAGNETIC ACADEMY

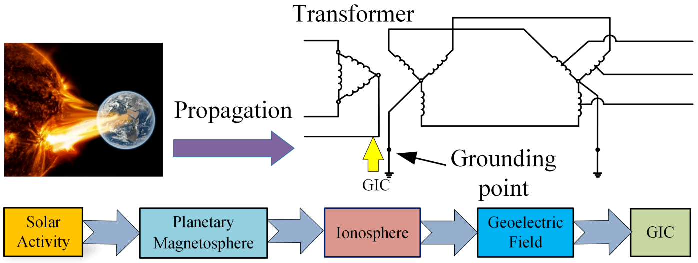

**FIGURE 1.** Path of GIC intrusion.

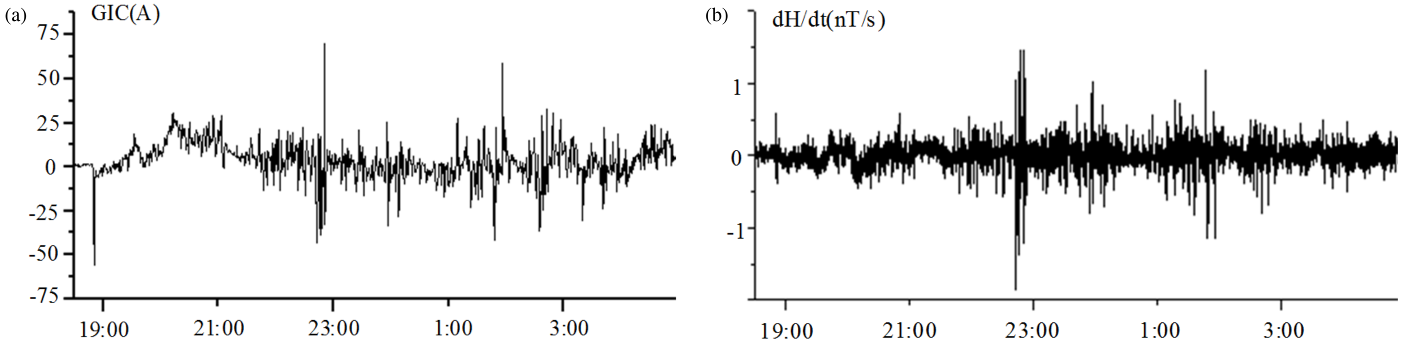

**FIGURE 2.** Monitoring data of substation and geomagnetic station on typical magnetic storm day. (a) Neutral point current of the 1# main transformer. (b) Rate of change of the horizontal component of the geomagnetic field.

and acoustic domains is proposed in this paper. Thus, the key parameters of transformer under GIC interference can be obtained.

Based on the multi-physics coupling principle, the time-domain characteristic of GIC is investigated. By analyzing substation data, GIC can be regarded as being composed of continuous DC component and intermittent distortion component. Then, typical distortion degrees and distortion time are selected to quantify the characteristic of distortion component. A three-dimensional simulation model is established to obtain key parameters of electromagnetic, mechanical, and acoustic domains, and the variation laws are analyzed. Dynamic experiment platforms are built to measure current, vibration, and noise under different scenarios. By comparing simulation results with experimental data, the correctness of method and conclusions are verified. On this basis, the mapping relationship between GIC distortion rate and noise is constructed. Thus, the unobservable physical features can be deduced from measurable electrical parameters.

## 2. CHARACTERISTICS OF GIC

Solar activity mainly affects the space magnetic field in the ionosphere at altitudes of 100 to 150 km through geomagnetic activity, which leads to changes in the ground-induced electric field. Subsequently, GIC is formed in the grounding transformer and earth loop [18]. This process is shown in Fig. 1.

Studies have shown that GIC leads to over excitation saturation, and the magnetostrictive effect of silicon steel sheets is aggravated in [19, 20]. Additionally, the vibration of core and winding is intensified by the distorted current and magnetic leakage. Internal components are caused to loosen, deform, or fall off, thus reducing the mechanical and electrical strength of transformer. Meanwhile, the intensified vibration can also lead to more severe noise.

The measured data from the nuclear power plant and geomagnetic station [21] are shown in Fig. 2. The neutral point current data of the 1# main transformer on typical magnetic storm days are shown in Fig. 2(a). At the same time, the changes in the horizontal component of the geomagnetic field are presented in Fig. 2(b). The information shows that the neutral point current is mainly caused by GIC resulting from solar activity.

A typical segment of the current waveform in Fig. 2(a) is selected as shown in Fig. 3. Thus, the time-domain variation of GIC is learned, and it is observed that the current fluctuates

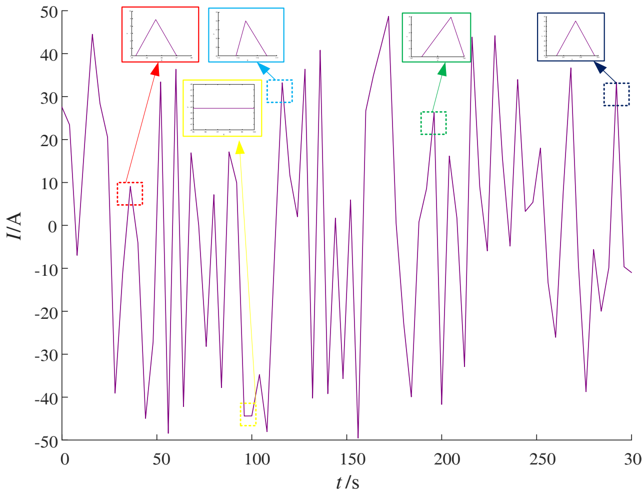

**FIGURE 3.** Time-domain variation of GIC.

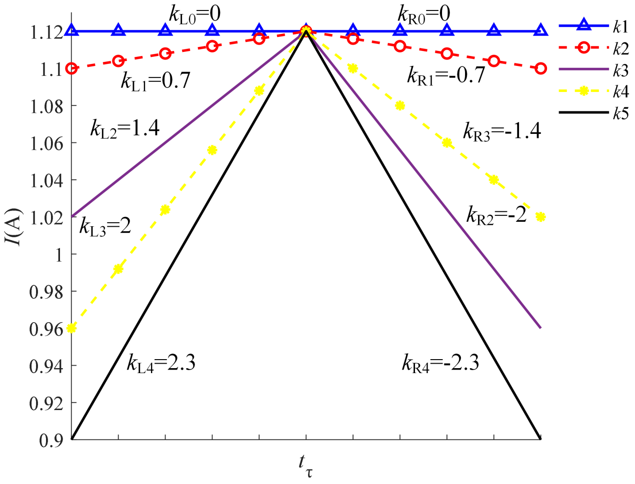

**FIGURE 4**. Typical waveform of GIC.

irregularly with intermittent impulse. During these impulse periods, current rapidly surges to a peak (defined as the inflection point) and then sharply drops. The moment when current reaches the peak is defined as the distortion time $t_\tau$.

The further analysis of GIC characteristics is carried out. Change rates are defined: the ascending rate (on the left side of $t_\tau$) $k_L$ and descending rate (on the right side of $t_\tau$) $k_R$. The typical distortion of current is shown in Fig. 4. The distortion time $t_\tau$ and distortion rate $\Delta k$ are defined to characterize the time-domain fluctuation of GIC.

$$\left.\begin{aligned} t_\tau &= \theta + \tau \\ \Delta k &= k_L - k_R \end{aligned}\right\} \tag{1}$$

where $\theta$ is the initial phase of the power frequency excitation of the transformer, and $\tau$ is the phase angle difference between $t_\tau$ and initial phase of the power frequency excitation.

When $\Delta k = 0$, the waveform is a straight line, so GIC can be regarded as a DC component. For other values of $\Delta k$, the waveform appears as a sharp wave, and GIC is considered distortion component. Thus, GIC can be characterized as a combination of DC component and distortion component. Analysis of current data shows that the amplitude and proportion of DC component are significantly smaller than those of distortion component.

## 3. ANALYSIS OF MULTI-PHYSICS COUPLING UNDER GIC INTERFERENCE

### 3.1. Electromagnetic Domain

A three-phase transformer circuit model, considering the GIC disturbance $i_{GIC}$ and secondary-side circulation $i_{cn}$, is shown in Fig. 5, and it comprises the primary-side parameters ($u_A$, $u_B$, $u_C$, $i_A$, $i_B$, $i_C$, $z_1$) and the secondary-side parameters ($u_a$, $u_b$, $u_c$, $i_a$, $i_b$, $i_c$, $i_{a1}$, $i_{b1}$, $i_{c1}$, $z_2$).

Under GIC interference, the winding current can be expressed as the superposition of distortion quantities $i_{GIC}$ with alternating quantities $i_{ac}$. The magnetic flux can also be represented by distortion quantities $\Phi_{GIC}$ and alternating quantities $\Phi_{ac}$. The winding current and main flux deviate from the power frequency, when GIC changes.

$$\left.\begin{aligned} i(t) &= i_{GIC}(t) + i_{ac}\sin(\omega t + \theta) \\ \Phi(t) &= \Phi_{GIC}(t) + \Phi_{ac}\sin(\omega t + \theta) \end{aligned}\right\} \tag{2}$$

where $\omega$ is the angular frequency.

$$\mathbf{J}_{in} = \mathbf{J}_{GIC}\left(t_\tau, \Delta k\right) + \mathbf{J}_{ac}\left(t, \theta\right) \tag{3}$$

where $\mathbf{J}_{in}$ is the magnetizing current density, which is the superposition of the power frequency current density $\mathbf{J}_{ac}$ and GIC density $\mathbf{J}_{GIC}$. By incorporating $\mathbf{J}$, a magnetic field model under GIC interference is constructed, and it is solved by the Galerkin method of weighted residuals [22].

$$\begin{aligned} G_{in} = &\int \nabla\times M_m\cdot\left(\frac{1}{\mu}\nabla\times A\right) d\mathbf{V} - \int M_m\cdot J_{GIC}\left(t_\tau, \Delta k\right) d\mathbf{V} \\ &- \int M_m\cdot J_{ac}\left(t, \theta\right) d\mathbf{V} - \int M_m\cdot\left[\left(\frac{1}{\mu}\nabla\times A\right)\times n\right] d\mathbf{S} \end{aligned} \tag{4}$$

where $G_{in}$ is the Galerkin residual under GIC interference. $\mu$ is the permeability; $\mathbf{A}$ is the magnetic vector potential; $\mathbf{M}_m$ is the weight function, which matches the basis function; $\mathbf{n}$ is the normal component. Then, $A$ and some field parameters can be calculated by discretizing the $G_{in}$ equation, such as magnetic flux density $\mathbf{B}$ and magnetic field energy $dW_m$ (see Appendix A).

### 3.2. Magneto-Mechanical Coupling

The axial force unit model of winding is established [23], as shown in Fig. 6. Then, the axial electromagnetic force and vibration are mainly analyzed in this paper.

Considering the stiffness characteristic of the insulating plate and winding coil, when the pre-tightening force is fixed, the material parameters can be regarded as linear [24]. Through the electromagnetic interference domain, the electromagnetic force can be calculated.

$$\mathbf{F}_e = \sum^{n_s} \int \mathbf{J}_{in} \times \mathbf{B} dV \tag{5}$$

where $n_s$ is the total number of units of a single winding coil. Consequently, the electromagnetic force $\mathbf{F}_{in}$ on the winding units under GIC interference can be derived:

$$\mathbf{F}_{in} = \mathbf{F}_{ac} + \mathbf{F}_{GIC} = 0.5\mathbf{B}I_m^2(1 + \cos 2\omega t) + \mathbf{F}_{GIC}(t, \Delta k) \tag{6}$$

During normal operation, the change cycle of the force is 0.5 times of the power frequency cycle. Under GIC interference, the force includes twice of the power frequency and GIC component.

The core vibration is primarily caused by the magnetostrictive effect in operation [25, 26]. The equivalent model of the core vibration under GIC interference is illustrated in Fig. 7. The sine excitation $i_{ac}$ causes the ferromagnetic substance to increase by $\Delta L_{ac}$, and the geomagnetically induced excitation

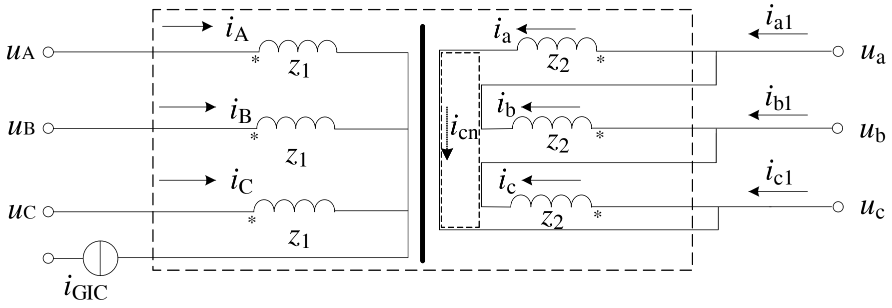

**FIGURE 5.** Circuit diagram under GIC interference.

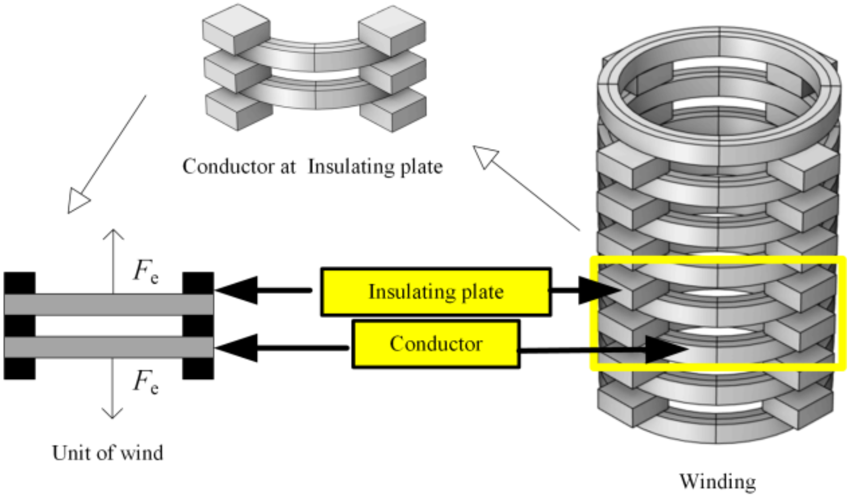

**FIGURE 6.** The basic unit of winding after simplification.

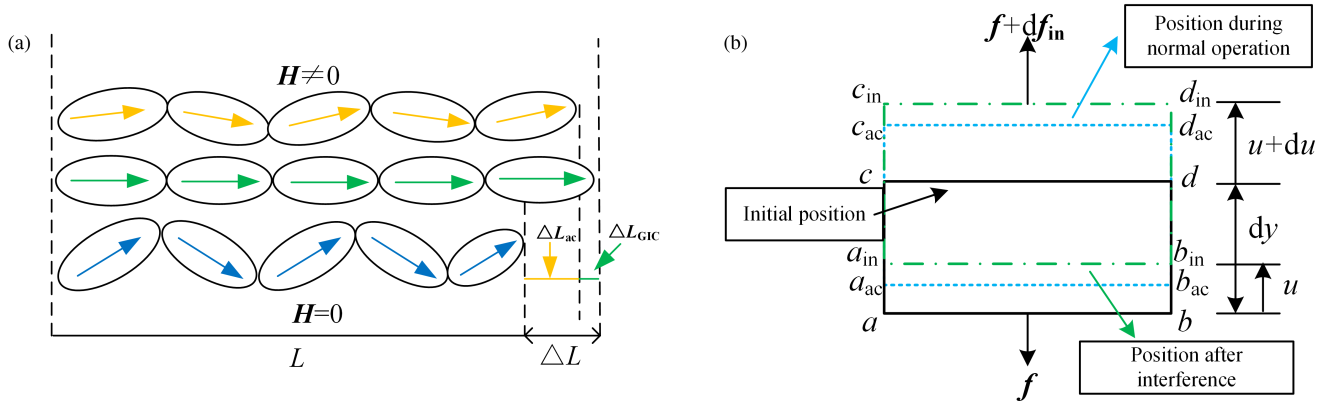

**FIGURE 7.** Fundamental principles of core vibration. (a) The basic principle of magnetostrictive effect under GIC interference. (b) Equivalent model of core unit under GIC interference.

$i_{GIC}$ causes an increase of $\Delta L_{GIC}$. Therefore, the magnetostrictive coefficient $\varepsilon_{in}$ can be deduced:

$$\varepsilon_{in} = \frac{\Delta L_{ac} + \Delta L_{GIC}}{L} \tag{7}$$

In the magnetostrictive effect, the following relationships exist among the relative permeability, stress, and magnetic flux density:

$$\left.\begin{aligned} \Delta\mu &= -\frac{2\varepsilon_b \sigma \mu^2}{\mathbf{B}_n^2} \\ \mathbf{B}_e &= (\mu + \Delta\mu)\mathbf{H} + \varepsilon\sigma \end{aligned}\right\} \tag{8}$$

where $\Delta\mu$ is the relative permeability, $\sigma$ the stress, $\varepsilon_b$ the magnetostrictive coefficient under magnetic saturation, and $\mathbf{B}_n$ and

$\mathbf{B}_e$ are the magnetic flux density in the saturated state and under stress, respectively.

$\mathbf{f} + d\mathbf{f_{in}}$ is the force acting on the cross-section of the core unit. The vibration equation of the core column is given [20]:

$$ES_c \frac{\partial^2 \mathbf{s}(y,t)}{\partial y^2} + \mathbf{f}(y,t) = \rho_c S_c \frac{\partial^2 \mathbf{s}(y,t)}{\partial t^2} \tag{9}$$

where $E$ is the Young's modulus, $\partial \mathbf{s}/\partial y$ the axial strain, $\mathbf{f}(y,t)$ the magnetostrictive force which is related to the position $y$ and time $t$, $\rho_c$ the core density, $S_c$ is the core's cross-sectional area. $\mathbf{s}$ is the core's axial displacement.

Based on the mechanical propagation domain, the vibration acceleration $g_{in}$ of the components under GIC interference can be calculated.

$$g_{in} = d^2\mathbf{s}/dt^2 \tag{10}$$

### 3.3. Mechanical-Acoustic Coupling

Taking $g_{in}$ as the propagation excitation source of the acoustic model, the coupled calculation can be realized in sound field.

$$\left.\begin{aligned} -n \cdot \left(-\frac{1}{\rho_a}(\nabla p_t - q_d)\right) &= -\,n \cdot g_{in} \\ p_t &= p_b + p \end{aligned}\right\} \tag{11}$$

where $\rho_a$ is the air fluid density, $p_t$ the total sound pressure, $p_b$ the background sound pressure, $p$ the noise sound pressure of transformer, and $q_d$ the dipole domain source.

Based on the solid-fluid propagation principle and combined with above parameters, the changes in the acoustic field close to transformer under GIC interference can be calculated. Additionally, the sound pressure level $L_p$ can be solved.

$$L_p = 20 \cdot \lg\left(\frac{P}{P_{ref}}\right) \tag{12}$$

where $L_p$ is measured in decibels (dB); $P$ is the valid value of sound pressure; $P_{ref}$ is generally set as 20 μPa for the reference sound pressure.

The principle of multi-physics coupling is illustrated in Fig. 8.

**TABLE 1**. Distortion parameters of GIC.

| Mode \ Parameters | | $k_L$ | $k_R$ | $\Delta k$ |
|---|---|---|---|---|
| Normal | $k_0$ | - | - | - |
| Under GIC interference | $k_1$ | 0 | 0 | 0 |
| | $k_2$ | 0.7 | −0.7 | 1.4 |
| | $k_3$ | 1.4 | −2 | 3.4 |
| | $k_4$ | 2 | −1.4 | 3.4 |
| | $k_5$ | 2.3 | −2.3 | 4.6 |

## 4. SIMULATION

Taking the three-phase transformer (JSSG-15 kVA 380 V/110 V) as an example, the experimental transformer is shown in Fig. 14, and the parameters are listed in Table 2.

### 4.1. Pre-Procedure

In order to reduce complexity, the following simplifications are made for the model:

i The material parameters of winding and core are obtained through tensile-compression tests and linearized. [21] (see Table 2).

ii The influence of core tie plates and clamping pieces on electromagnetic and mechanical domain is ignored.

iii The air gap among the platens, clamps, and winding coils is disregarded.

The following is applied to the excitation and boundary:

i A circular current is used as the winding excitation in electromagnetic interference domain. Parallel magnetic lines are set as the magnetic field boundary conditions. Other boundary conditions are set as natural boundaries.

ii In mechanical vibration propagation domain, the roller support is applied to the transformer base. Considering the axial vibration of components, fixed constraints are applied to the other parts.

iii In acoustic propagation domain, the background sound pressure is set to 0 Pa. With the domain boundary condition set as spherical wave radiation, the environmental noise has no impact on the sound pressure.

With GIC interference, different scenarios are set up:

*Scenario I*: No GIC interference, $i_{GIC} = 0$ ($k_0$ in Table 1).

*Scenario II*: During the interval phase of GIC interference, $i_{GIC}$ is DC component ($k_1$ in Fig. 4).

*Scenario III*: During the impulse phase of GIC interference, $i_{GIC}$ is distortion component ($k_{2\sim5}$ in Fig. 4).

Taking phase B as an example, the phase angle of $i_B$ is set to 0°. The value of $i_{GIC}$ is scaled proportionally to match the transformer, based on measured data. In order to simulate GIC interference in the situation when $i_B$ is zero or reaches its maximum or minimum values, the phase difference $\tau$ of $i_{GIC}$ is set to 0°, ±90°, respectively. Meanwhile, the load factor $\eta$ is set to 0, 25%, 50%, 75%, and 100% depending on different load conditions. Thus, the variations in magnetic field, vibration, and noise are analyzed.

The distribution of test points in phase B considers the structural characteristics of components, as shown in Fig. 9.

### 4.2. Simulation and Analysis of Winding

Under different scenarios, the magnetic leakage at test point ① is simulated, which are shown in Fig. 10. Partial results of current and main magnetic flux in phase B are presented in the appendix.

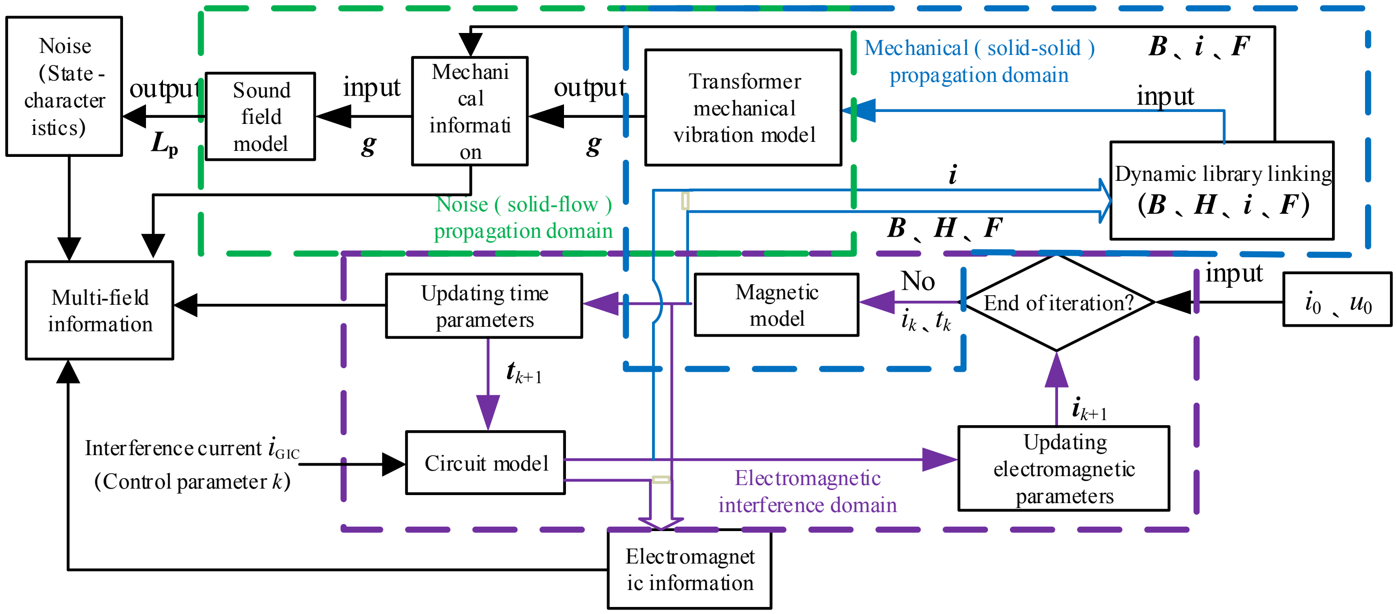

**FIGURE 8**. The principle of multi-physics coupling under GIC interference.

**TABLE 2**. Transformer parameters.

| Parameters | Rated value | Measured value |
|---|---|---|
| Capacity $S_N$ (kVA)/Frequency (Hz) | 15/50 | — |
| High/low winding voltage $U_N$/V | 380/$\sqrt{3}$/110 | — |
| No-load current $I_0$/A | 4.2% | — |
| Core size /mm | — | 550 × 216 × 545 |
| Winding height/mm | — | 370 |
| Young's modulus of silicon steel sheet | 1.95 | 1.93 |
| Poisson's ratio of silicon steel sheet | 0.27 | 0.26 |
| Young's modulus of winding coils | 0.81 | 0.80 |
| Young's modulus of winding coils | 0.36 | 0.35 |

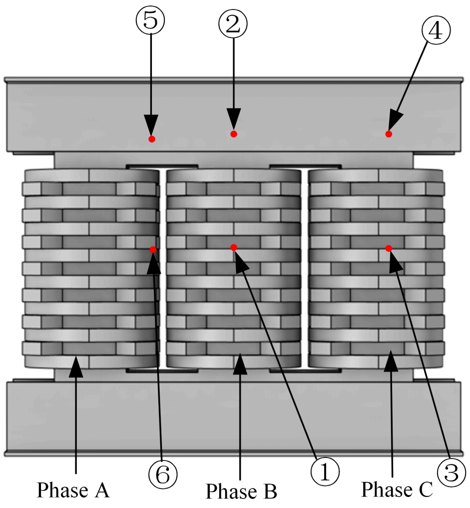

**FIGURE 9**. Virtual simulation model.

Analysis reveals that under normal no-load conditions, the waveform of primary current is a peaked wave, and during loaded operation it is a sinusoidal wave. In Scenario II with magnetic bias caused by DC disturbance, no-load current exhibits "half-wave distortion" (front-half amplification and rear-half attenuation), while loaded current remains unaffected. Results in Scenario III show that the period of winding current exhibits shortening during the $k_L$-phase and prolongation in the $k_R$-phase. Significant current fluctuations emerge at $t_\tau$ instant, which exhibits a positive correlation with $\Delta k$. Serious interference occurs when $t_\tau$ ($\tau = 90°$ ) coincides with the instant of peak current magnitude.

As shown in Fig. 10, magnetic leakage exhibits "half-wave distortion" under no-load. Under load, magnetic leakage increases with the growth of $\eta$. In Scenario 3, the fluctuation period of magnetic leakage deviates from the power frequency, particularly showing severe distortion at $t_\tau$ instant. Moreover, the distortion becomes more aggravated with the increase of $\Delta k$. When $\tau = 90°$, the impact of GIC distortion on magnetic leakage is most significant. Analysis reveals that magnetic leakage is mainly induced by alternating current in winding, so its variation basically aligns with the current's variation.

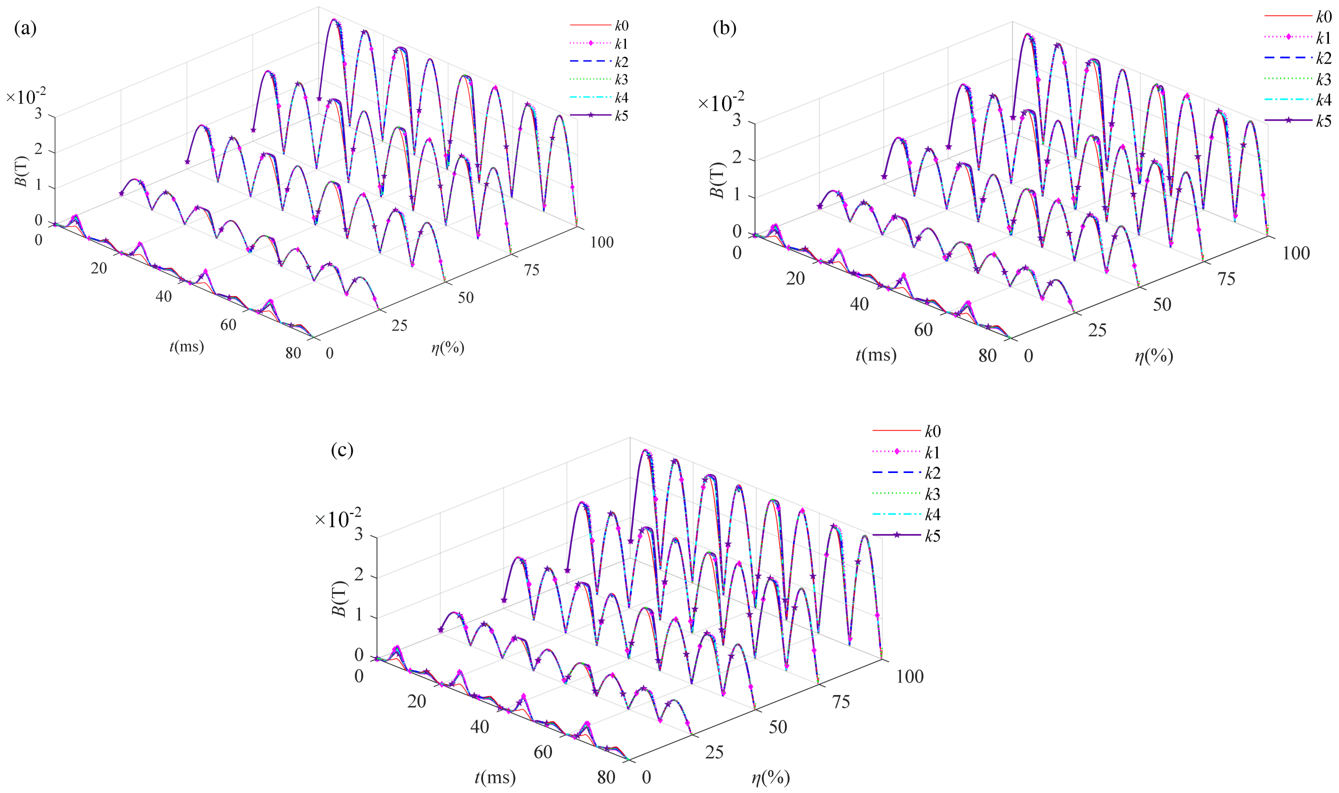

**FIGURE 10**. Magnetic leakage information of test point ①. (a) $\tau = 0$, (b) $\tau = 90^\circ$, (c) $\tau = -90^\circ$.

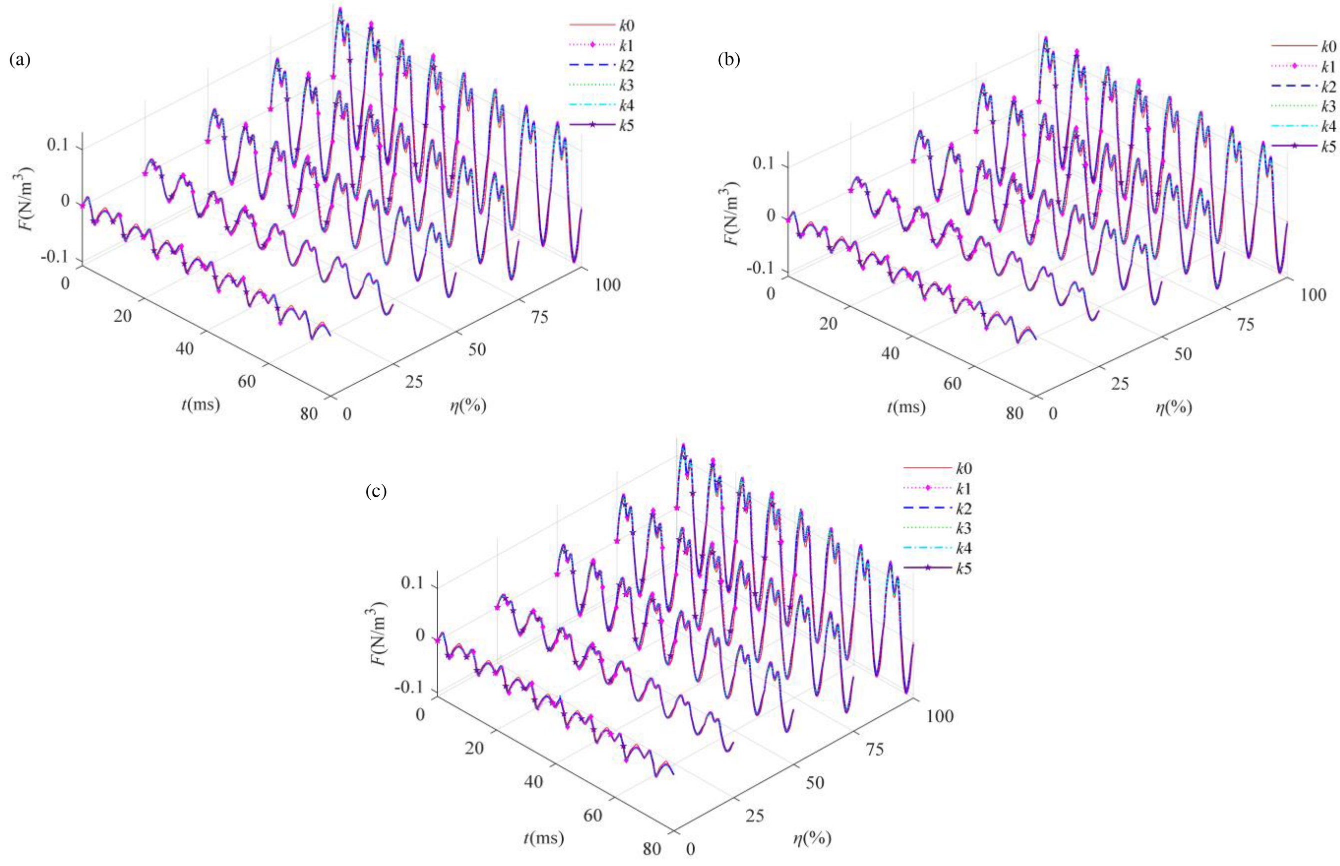

**FIGURE 11**. Force information of test point ①. (a) $\tau = 0$, (b) $\tau = 90^\circ$, (c) $\tau = -90^\circ$.

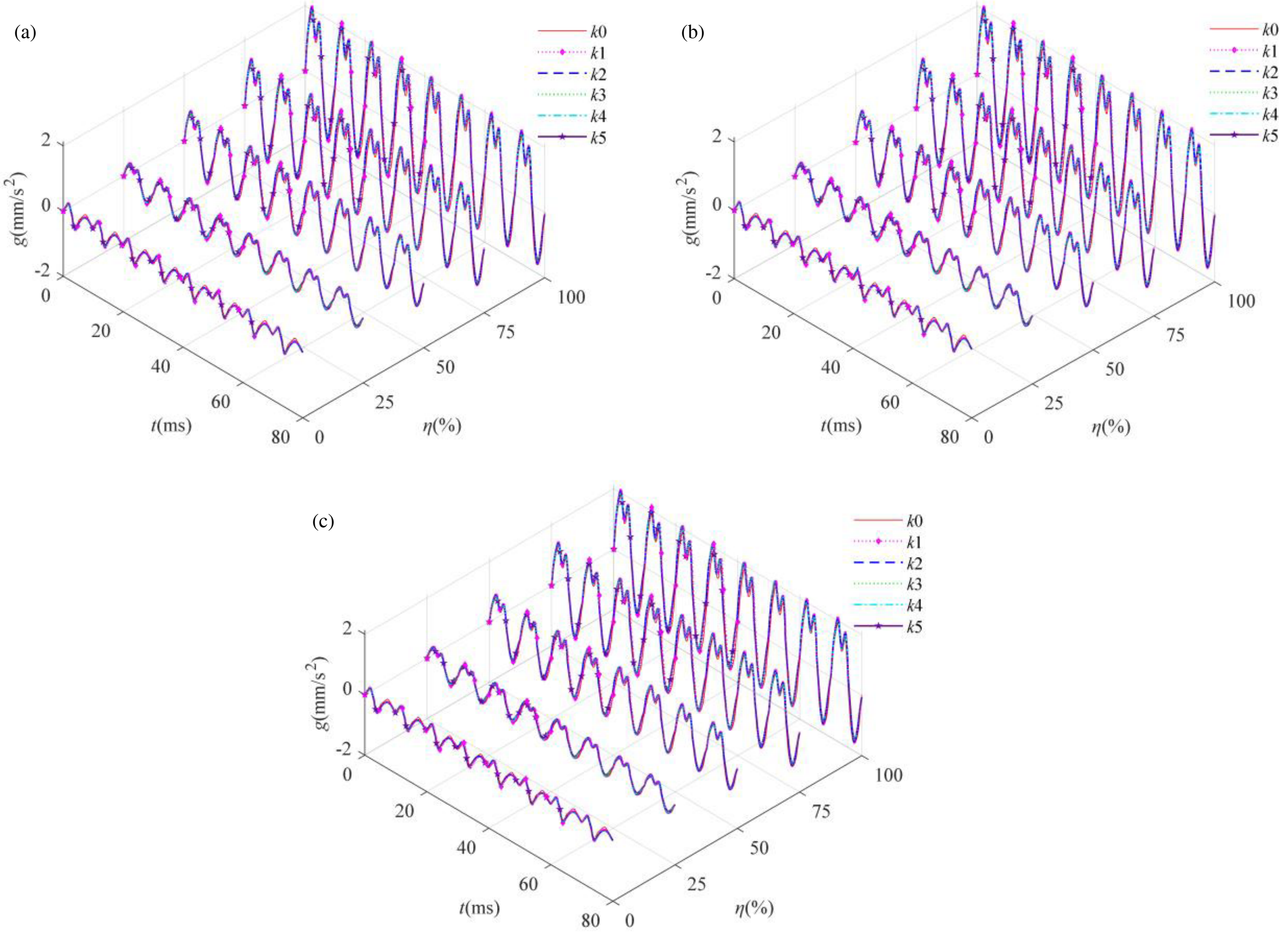

**FIGURE 12**. Vibration information of test point ①. (a) $\tau = 0$, (b) $\tau = 90°$, (c) $\tau = -90°$.

The electromagnetic force and vibration acceleration at test point ① are analyzed. The results are shown in Figs. 11 and 12.

As depicted in Figs. 11 and 12, the fluctuation periods of electromagnetic force and vibration acceleration in Scenarios I and II are equal to half of the power frequency excitation. And it is consistent with derivations in Equation (6). In Scenario III, the variation period of these parameters at test point deviates from half of the power frequency cycle. At $t_\tau$ instant, the fluctuation intensity of winding mechanical force becomes more severe with increasing $\Delta k$. The most interference emerges when $\tau = 90°$. The analysis of Figs. 10–12 indicates that the magnetic leakage, force, and vibration exhibit similar variation laws. The mechanism lies in the forced vibration of winding driven by periodic electromagnetic force within magnetic leakage field. Notably, GIC distortion component exhibits stronger impact on winding than DC component.

## 4.3. Simulation and Analysis of Core

The simulation analysis on the variation of core vibration under different scenarios is carried out, and results are shown in Fig. 13.

As illustrated in Fig. 13, core vibration exhibits higher complexity and intensity than winding vibration. Under identical $\eta$, comparative analysis between Scenarios I and II reveals core vibration intensifies significantly when the transformer is affected by DC component. Comparing Scenarios II and III, when being subjected to the distortion component, the vibration signal distorts at $t_\tau$ instant. As $\Delta k$ increases, the core vibration at $t_\tau$ instant becomes more severe, and the fluctuation is the most prominent when $\tau = 90°$.

## 4.4. Simulation and Analysis of Noise

The maximum sound pressure levels (defined as $L_{pmax}$) on the surface of transformer are simulated, as shown in Tables 3–5.

Analysis of each scenario reveals a positive correlation between $L_{pmax}$ and $\eta$. In Scenario III, $L_{pmax}$ grows as $\Delta k$ increases. Under equivalent $\eta$ conditions, maximum $L_p$ is observed when $\tau = 90°$, and it is approximately 10% higher than that under normal conditions.

Through simulations, the impact of GIC distortion on multi-physical fields of transformer is analyzed. Then, the variation laws can be summarized:

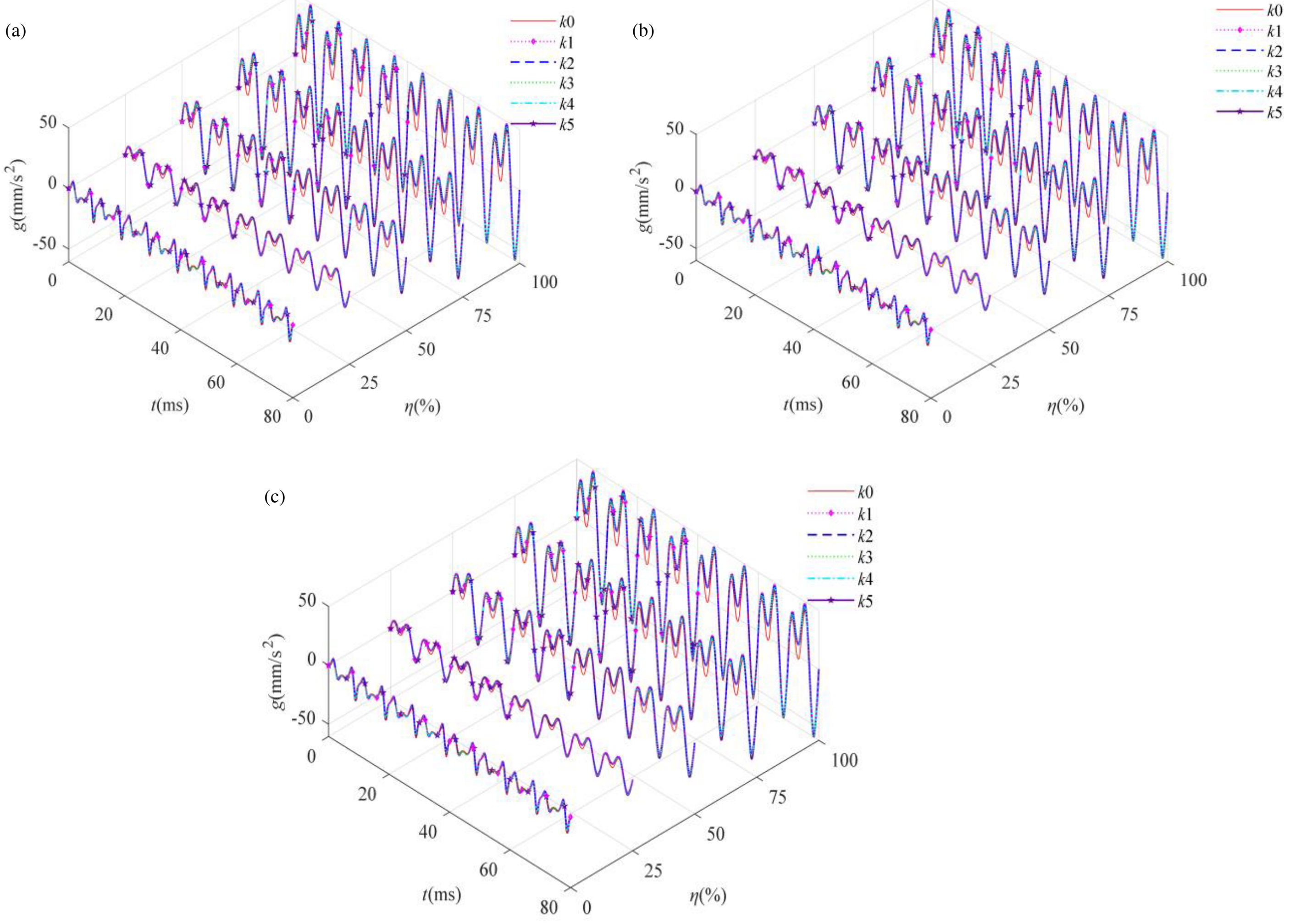

**FIGURE 13**. Vibration information of test point ①. (a) $\tau = 0$, (b) $\tau = 90°$, (c) $\tau = -90°$.

**TABLE 3**. Maximum surface noise of transformer at $\tau = 0$.

| State<br>Noise | Scenario | | Load Factor $\eta$ (%) | | | | |
|---|---|---|---|---|---|---|---|
| | | | 0 | 25 | 50 | 75 | 100 |
| $\mathbf{L_{pmax}}$ **(dB)** | Scenario I | $k_0$ | 26.8 | 27.5 | 27.6 | 28.7 | 29.7 |
| | Scenario II | $k_1$ | 27.6 | 28.5 | 29.4 | 30.2 | 31.3 |
| | Scenario III | $k_2$ | 28.1 | 28.8 | 29.7 | 30.6 | 31.8 |
| | | $k_3$ | 28.3 | 29 | 29.9 | 31.0 | 32.2 |
| | | $k_4$ | 28.3 | 29.2 | 30.0 | 31.1 | 32.2 |
| | | $k_5$ | 28.9 | 29.8 | 30.6 | 31.8 | 32.9 |

$i$: Under GIC interference, the magnetic leakage, electromagnetic force, vibration acceleration, and current all exhibit similar variation laws. The variations are more significant under no-load conditions, with multi-field parameters manifesting "half-wave distortion". In contrast, under load conditions, the fluctuations of parameters are relatively small. Further analysis indicates that the impact on vibration and noise becomes greater with increasing $\Delta k$.

$ii$: The most severe impact occurs when the instant of peak power-frequency current coincides with $t_\tau$. As $\eta$ increases, the multi-field parameters also increase. Analysis shows that core vibration is more complex and intense than winding vibration under identical scenario, which indicates that core is more sus-

**TABLE 4**. Maximum surface noise of transformer at $\tau = 90°$.

| **State** <br> **Noise** | **Scenario** | | **Load Factor $\eta$ (%)** | | | | |
|---|---|---|---|---|---|---|---|
| | | | 0 | 25 | 50 | 75 | 100 |
| **$L_{pmax}$** (dB) | Scenario I | $k_0$ | 26.8 | 27.5 | 27.6 | 28.7 | 29.7 |
| | Scenario II | $k_1$ | 27.6 | 28.5 | 29.4 | 30.2 | 31.3 |
| | Scenario III | $k_2$ | 28.3 | 29 | 29.9 | 31.0 | 32.3 |
| | | $k_3$ | 28.6 | 29.5 | 30.3 | 31.4 | 32.6 |
| | | $k_4$ | 28.7 | 29.6 | 30.4 | 31.5 | 32.7 |
| | | $k_5$ | 29.3 | 30.2 | 31.1 | 31.9 | 33.1 |

**TABLE 5**. Maximum surface noise of transformer at $\tau = -90°$.

| **State** <br> **Noise** | **Scenario** | | **Load Factor $\eta$ (%)** | | | | |
|---|---|---|---|---|---|---|---|
| | | | 0 | 25 | 50 | 75 | 100 |
| **$L_{pmax}$ (dB)** | Scenario I | $k_0$ | 26.8 | 27.5 | 27.6 | 28.7 | 29.7 |
| | Scenario II | $k_1$ | 27.6 | 28.5 | 29.4 | 30.2 | 31.3 |
| | Scenario III | $k_2$ | 28.1 | 28.8 | 29.5 | 30.6 | 31.8 |
| | | $k_3$ | 28.3 | 29 | 29.9 | 30.9 | 32.3 |
| | | $k_4$ | 28.4 | 29.1 | 30 | 31.1 | 31.4 |
| | | $k_5$ | 29 | 29.9 | 30.5 | 31.6 | 32.9 |

ceptible to GIC. Under the same conditions, distortion component exerts a more significant impact than DC component.

## 5. EXPERIMENT

The dynamic experiment platform is built (as shown in Fig. 14), and the parameters of transformer are presented in Table 2. The steps are as follows:

*Step 1*: The voltage regulator and interference current modulation module are connected to the high-voltage side of transformer and link the adjustable load to the low-voltage side. The location of test points is consistent with those in simulation.

*Step 2*: Upon closing switch K, adjust the sliding rheostat $R_d$ to generate time-varying current from the module, thereby simulating various operational conditions through experiments. In Scenario III, difficulty arises in matching $t_\tau$ with power frequency excitation, which affects the accuracy of $\tau$. Additionally, challenges exist in determining $\Delta k$ for different modulation currents. Therefore, a large number of experiments are conducted to approximately simulate the interference effects of distortion component with $\tau = 0, \pm 90°$ and $\Delta k = 4.6$.

*Step 3*: Each monitoring module is utilized to gather current, vibration, and noise data under varying scenarios.

The vibration information of test points ① and ② in each scenario is shown in Fig. 15.

As depicted in Fig. 15, GIC distortion significantly affects the core. With increasing $\eta$, vibration is intensified. The spatiotemporal distribution and variation of experimental data exhibit higher complexity than simulation results. This complexity arises from the core's nonlinear excitation and magnetostrictive properties, resulting in a lot of high frequency components in vibration signal. The interactions of vibrations are further compounded by fastening and connecting components. Consequently, experimental waveform is more intricate and severe than simulation results.

The monitoring results of maximum noise in the transformer experiment are shown in Table 6.

As indicated in Table 6, the differences of $L_{pmax}$ under varying $t_\tau$ are not significant. It is attributed to measurement limitations such as environmental noise interference and instrumentation constraints. However, as $\eta$ exceeds 75%, the noise is approximately 1.1 times of that in normal situation. The findings demonstrate that GIC interference significantly amplifies $L_p$. Under identical circumstances, distortion component exerts a more pronounced influence than DC component. This observation aligns closely with simulation results.

A substantial quantity of experiments is carried out, and the results are compared with simulation. Thus, a mapping relationship between $\Delta k$ and $L_p$ on the surface of transformer is established.

Taking $\tau = 0$ as an example, the virtual-real information space is illustrated in Fig. 16. The correlation between $\Delta k$ and $L_p$ can be characterized by a mathematical function. For instance, when $\eta$ is 50, and $\tau$ is 0, the functional relationship between $\Delta k$ and $L_p$ can be simply fitted, which satisfies the virtual-real consistency verification.

$$\left.\begin{aligned} \text{Simulation}: L_p = 2.11 \times \Delta k + 28.74 \\ \text{Experiment}: L_p = 2.19 \times \Delta k + 29.68 \end{aligned}\right\} \tag{13}$$

Analysis demonstrates that the mapping relationship between $L_p$ and $\Delta k$ maintains consistent under different conditions of $\tau$ and $\eta$ (as presented in Appendix A). By leveraging $\Delta k$ as a critical indicator, a stability criterion considering operational

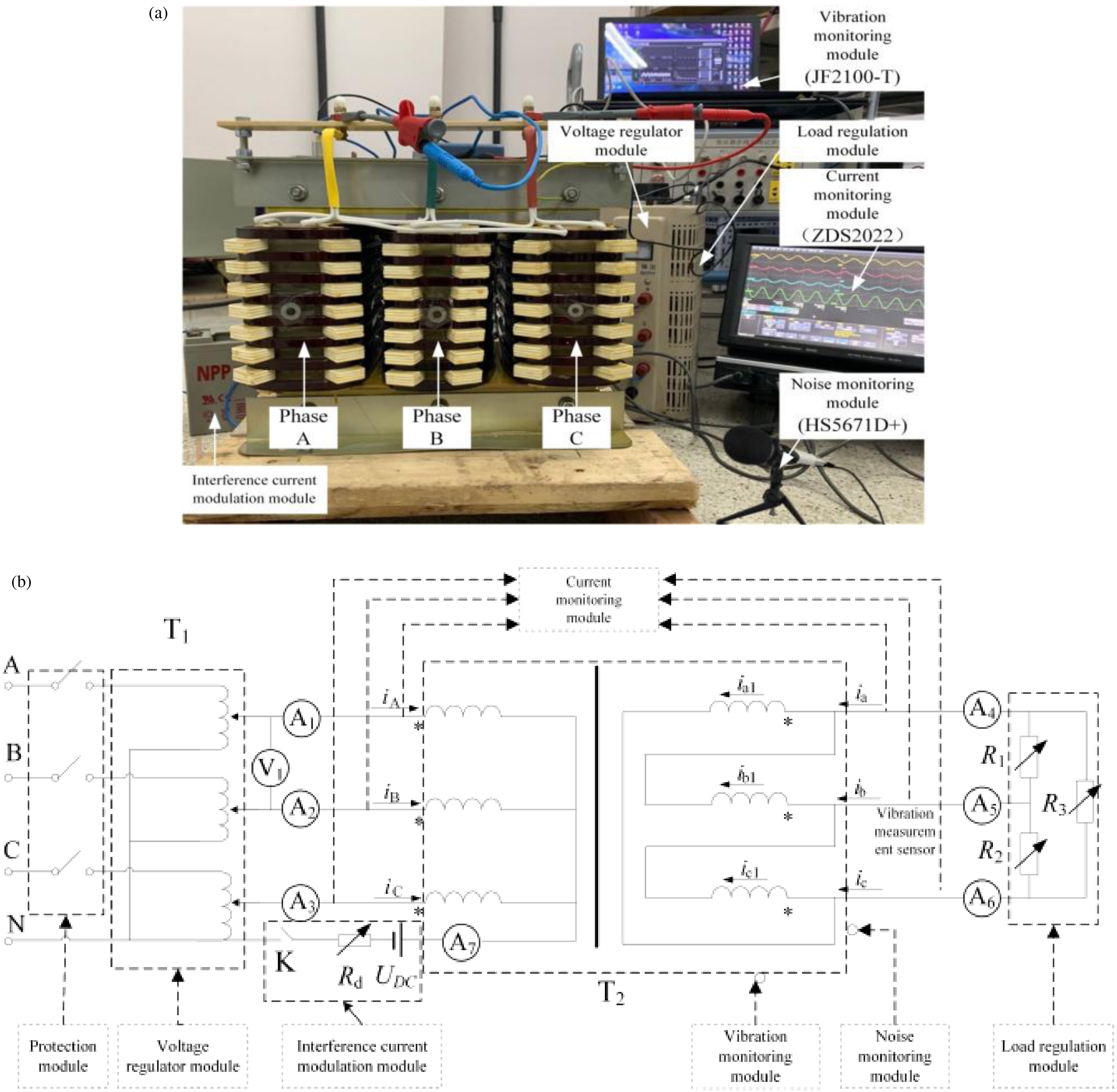

**FIGURE 14**. Experimental platform. (a) Physical experiment platform. (b) Wiring of experiment platform.

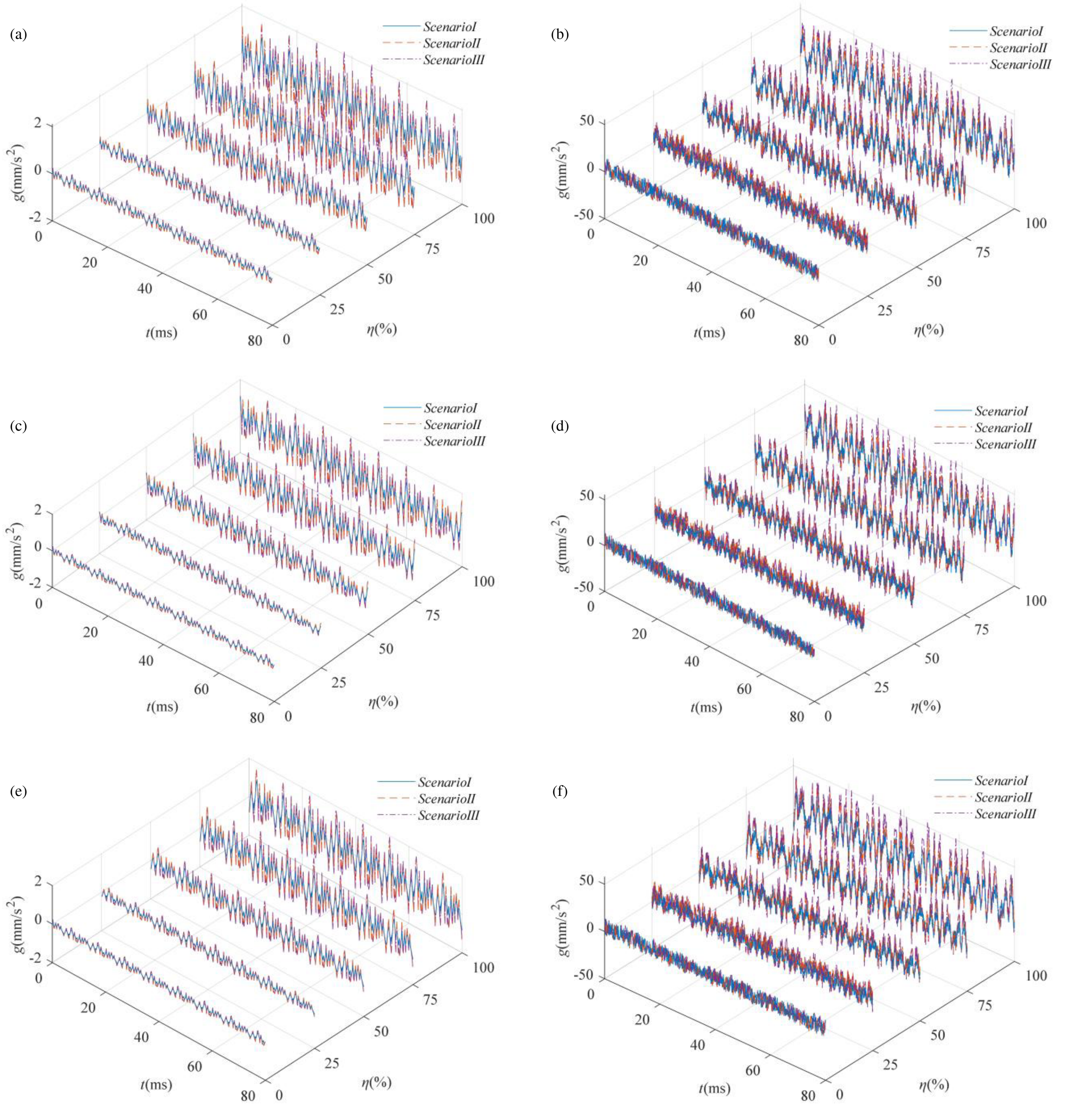

**FIGURE 15**. Vibration acceleration of component. (a) $\tau = 0$ at point ①. (b) $\tau = 0$ at point ②. (c) $\tau = 90^\circ$ at point ①. (d) $\tau = 90^\circ$ at point ②. (e) $\tau = -90^\circ$ at point ①. (f) $\tau = -90^\circ$ at point ②.

condition is established.

$$\Delta k = K_{rel}\Delta k_s \tag{14}$$

With predefined threshold ($\Delta k_s = 2.0$, $K_{rel} = 1.1$), this study establishes a stability criterion for GIC interference:

**Low-risk** ($0 < \Delta k \leq 1.25$): the influence of $i_{GIC}$ is relatively small, and transformer remains within the anti-interference capacity range.

**Moderate-risk** ($1.25 < \Delta k \leq 3$): vibration and noise increase notably, significantly impacting electromagnetic com-

**TABLE 6**. Maximum experiment noise of transformer.

| State / Noise | Scenario | | Load Factor $\eta$ (%) | | | | |
|---|---|---|---|---|---|---|---|
| | | | 0 | 25 | 50 | 75 | 100 |
| **$L_{pmax}$ (dB)** | Scenario I | | 29.3 | 30.7 | 31.1 | 32.3 | 33.1 |
| | Scenario II | | 31.4 | 31.9 | 32.4 | 33.3 | 34.6 |
| | Scenario III | $\tau = 0$ | 31.6 | 32.2 | 33.1 | 34.3 | 35.6 |
| | | $\tau = 90^\circ$ | 31.6 | 32.9 | 33.3 | 34.5 | 35.5 |
| | | $\tau = -90^\circ$ | 31.5 | 32.7 | 33.1 | 34.2 | 35.4 |

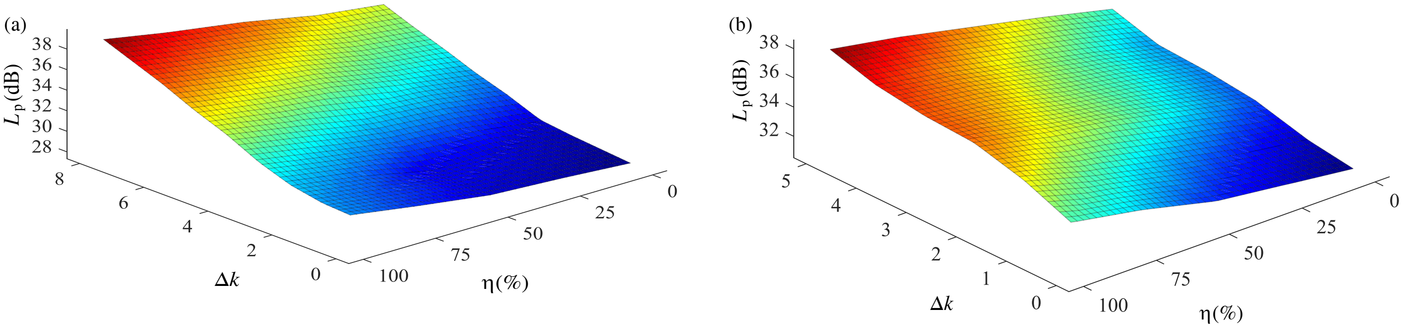

**FIGURE 16**. Mapping relationship of $L_p$-$\Delta k$. (a) Virtual simulation. (b) Physics experiment.

patibility and structural stability. Prompt attention and appropriate mitigation measures are necessary.

**Critical-risk** ($\Delta k > 3$): the influence of $i_{GIC}$ is more severe, leading to drastic changes in primary current and vibration. Immediate alarms and intervention are necessary.

Despite that $\eta$ typically stays below 75% and currents under GIC interference do not surpass the safety threshold, it can still induce internal environmental instability, adversely affecting components. In particular, GIC distortion component can abruptly escalate vibration and noise at "inflection point". When the instant of peak AC excitation coincides with $t_\tau$, more mechanical risks emerge. Conventional capacitor-based DC-blocking techniques show limited applicability due to GIC's long interference duration, stochastic distortion time, and low frequency. Relevant governance strategies and measures require further improvement.

## 6. CONCLUSION

Based on multi-field coupling, a model considering GIC is proposed. Thus, electromagnetism and abnormal physics effects of transformer under GIC are researched. The conclusions are as follows:

*i*: During GIC interference, the vibration and noise of core and winding vary drastically. The multi-physics parameters take periodic fluctuation as a "half-wave distortion" pattern. Furthermore, distortion component exerts a more significant impact on transformer than DC component.

*ii*: Under the same interference, vibration and noise grow with increasing $\Delta k$. Core is more susceptible to GIC than winding. The severest interference occurs when $t_\tau$ coincides with the peak instant of AC excitation. Thus, electromagnetic compatibility and structural stability of transformer will be damaged due to GIC.

*iii*: The vibration-acoustic morphology is investigated through multi-physics and multi-spatiotemporal scales. Avirtual mapping relationship is established to correlate measurable electrical parameters with unobservable physical features. Then, a stability criterion is proposed, providing a foundation for real-time situational awareness and full lifecycle maintenance strategies of power equipment.

## APPENDIX A.

$$\begin{bmatrix} G_x \\ G_y \\ G_z \end{bmatrix} = \int_\omega v \begin{bmatrix} \frac{\delta M_m}{\delta x}\left(\frac{\delta A_x}{\delta x} + \frac{\delta A_y}{\delta y} + \frac{\delta A_z}{\delta z}\right) \\ \frac{\delta M_m}{\delta y}\left(\frac{\delta A_x}{\delta x} + \frac{\delta A_y}{\delta y} + \frac{\delta A_z}{\delta z}\right) \\ \frac{\delta M_m}{\delta z}\left(\frac{\delta A_x}{\delta x} + \frac{\delta A_y}{\delta y} + \frac{\delta A_z}{\delta z}\right) \end{bmatrix} dV$$
$$+ \int_\omega v \begin{bmatrix} \frac{\delta M_m}{\delta y}\left(\frac{\delta A_y}{\delta x} - \frac{\delta A_x}{\delta y}\right) - \frac{\delta M_m}{\delta z}\left(\frac{\delta A_x}{\delta z} - \frac{\delta A_z}{\delta x}\right) \\ -\frac{\delta M_m}{\delta z}\left(\frac{\delta A_z}{\delta y} - \frac{\delta A_y}{\delta z}\right) + \frac{\delta M_m}{\delta x}\left(\frac{\delta A_y}{\delta x} - \frac{\delta A_x}{\delta y}\right) \\ -\frac{\delta M_m}{\delta x}\left(\frac{\delta A_x}{\delta z} - \frac{\delta A_z}{\delta x}\right) + \frac{\delta M_m}{\delta y}\left(\frac{\delta A_z}{\delta y} - \frac{\delta A_y}{\delta z}\right) \end{bmatrix} dV \tag{A1}$$

$$\mathbf{B} = \nabla \times \mathbf{A} \tag{A2}$$

According to the principle of energy balance, the change in magnetic field characteristic parameters caused by current excitation at the moment $t_k$ is:

$$dW_1 = \frac{1}{2}\int d\mathbf{B} \cdot d\mathbf{H} dV \tag{A3}$$

where **H** is the magnetic field intensity.

The change in winding current at this moment is $di_p/di_s$ (where $p$ represents A, B, C, and $s$ represents a, b, c).

$$dW_2 = \frac{1}{2} L_{ps} di_p di_s \tag{A4}$$

Set $W_1 = W_2$. By considering the magnetic field energy and circuit energy, the value of $\mathbf{L}$ can be calculated. Subsequently, substitute the inductance parameter at moment $t_k$ into the aforementioned differential equation. Furthermore, the current $i_{k+1}$ at the next moment within the circuit model via the fourth-order Runge-Kutta method can be solved:

$$i_{k+1} = i_k + \frac{h}{6}\left[s_1 + 2s_2 + 2s_3 + s_4\right] \tag{A5}$$

where $h$ is the step size, and $s_1$–$s_4$ is the slope of segmentation.

Under the condition of $\eta(\%) = 75$, $\tau = 0$, the mapping relationship of $L_p$ and $\Delta k$ is:

$$\left.\begin{aligned}\text{Simulation}: L_p = 2.115 \times \Delta k + 30.34\\ \text{Experiment}: L_p = 2.196 \times \Delta k + 32.18\end{aligned}\right\} \tag{A6}$$

Under the condition of $\eta(\%) = 100$, $\tau = 0$, the mapping relationship of $L_p$ and $\Delta k$ is:

$$\left.\begin{aligned}\text{Simulation}: L_p = 2.23 \times \Delta k + 32.82\\ \text{Experiment}: L_p = 2.36 \times \Delta k + 34.49\end{aligned}\right\} \tag{A7}$$

Under the condition of $\eta(\%) = 50$, $\tau = 90°$, the mapping relationship of $L_p$ and $\Delta k$ is:

$$\left.\begin{aligned}\text{Simulation}: L_p = 2.13 \times \Delta k + 29.16\\ \text{Experiment}: L_p = 2.196 \times \Delta k + 30.12\end{aligned}\right\} \tag{A8}$$

## APPENDIX B.

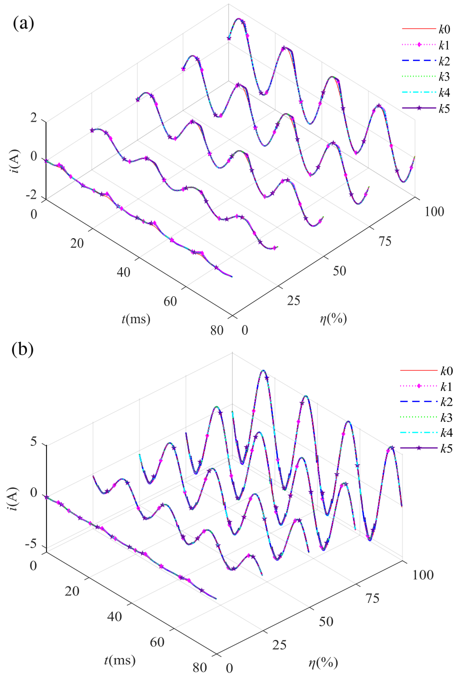

**FIGURE B1.** Simulation current of phase B at $\tau = \mathbf{0}$. (a) Primary side current. (b) Secondary side current.

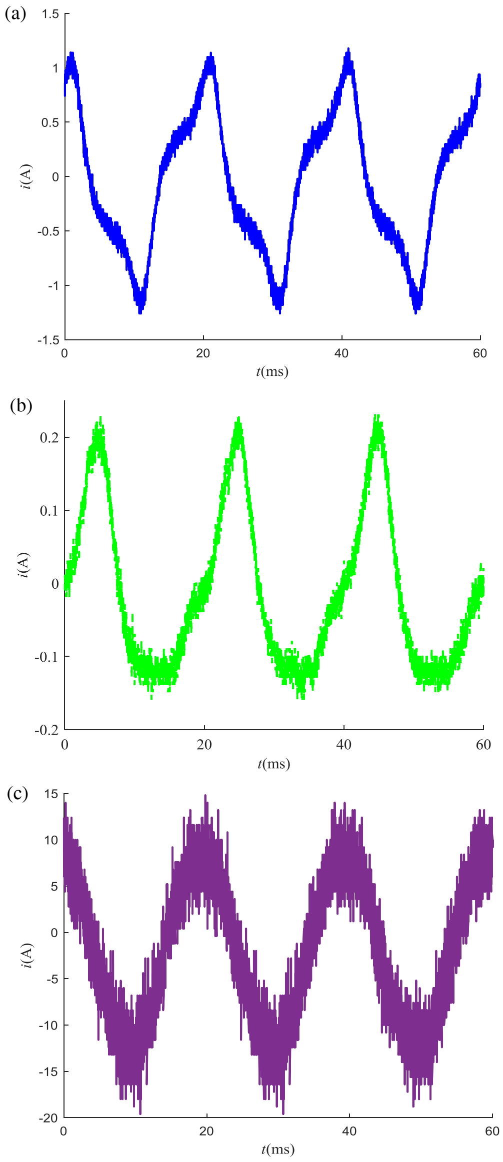

**FIGURE B2.** Measured current of phase B. (a) Current at $\eta = 0\%$ in Scenario I. (b) Current at $\eta = 0\%$ in Scenario II. (c) Current at $\eta = 50\%$ in Scenario I.

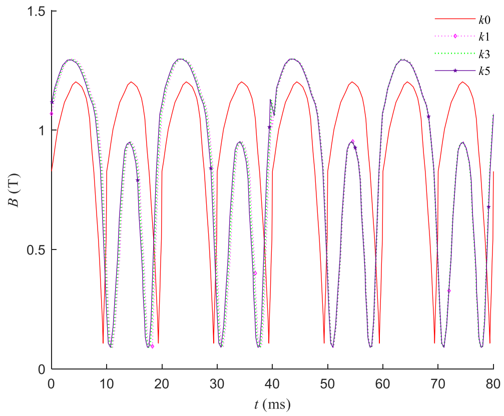

**FIGURE B3.** Main magnetic flux of phase B under no-load.

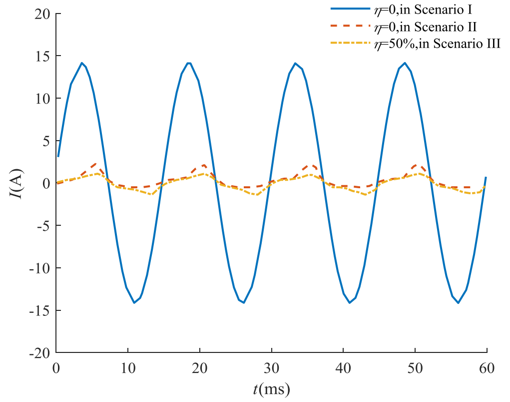

**FIGURE B4.** Measured current data of phase B after filtering.

## APPENDIX C.

A three-phase transformer (SFZ11-50000 kVA/110 kV) is taken as an example. The core size (mm) is 2180 × 3240 × 2465, and winding height (mm) is 1090. No-load current is 0.52% of the rated current. The results of simulations and experiments are listed below ($\tau = 0$, no-load).

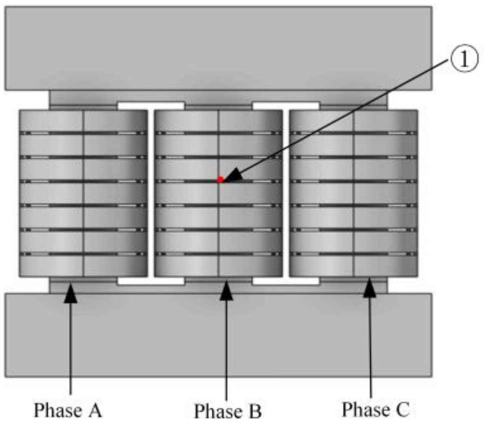

**FIGURE C1.** Virtual simulation model.

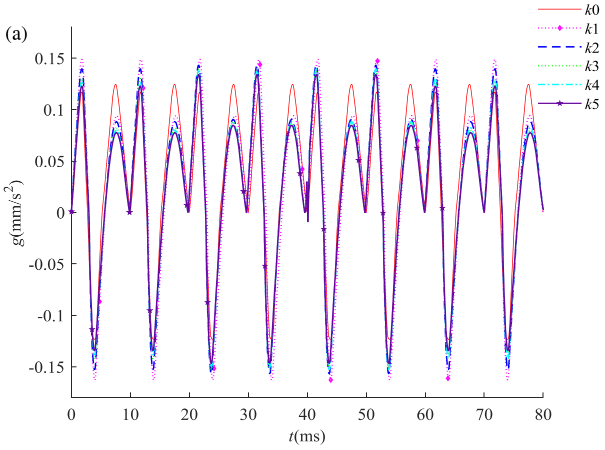

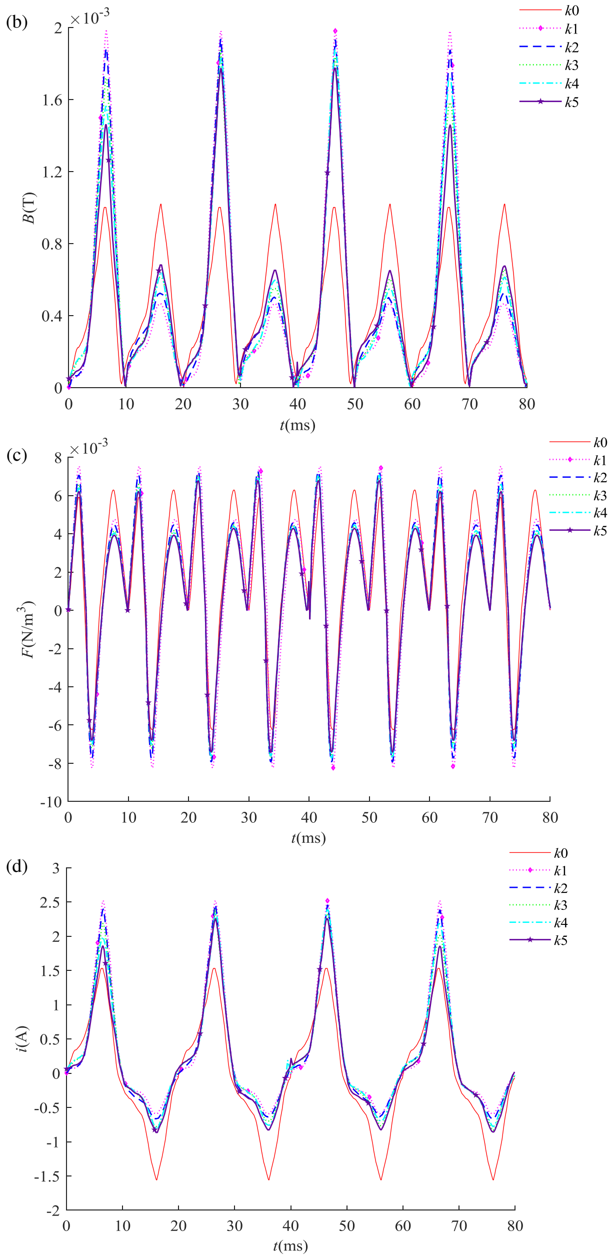

**FIGURE C2.** Simulation of phase B. (a) Vibration acceleration. (b) Magnetic leakage. (c) Force information. (d) Primary side current.

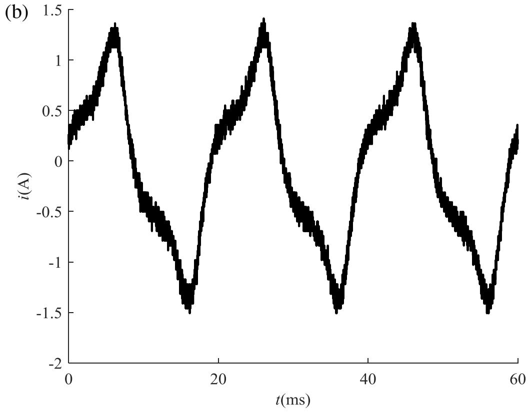

**FIGURE C3**. Measured data of phase B. (a) Field experiment. (b) No-load current.

A no-load current experiment is also conducted on a 10 kV transformer (10T35-3).

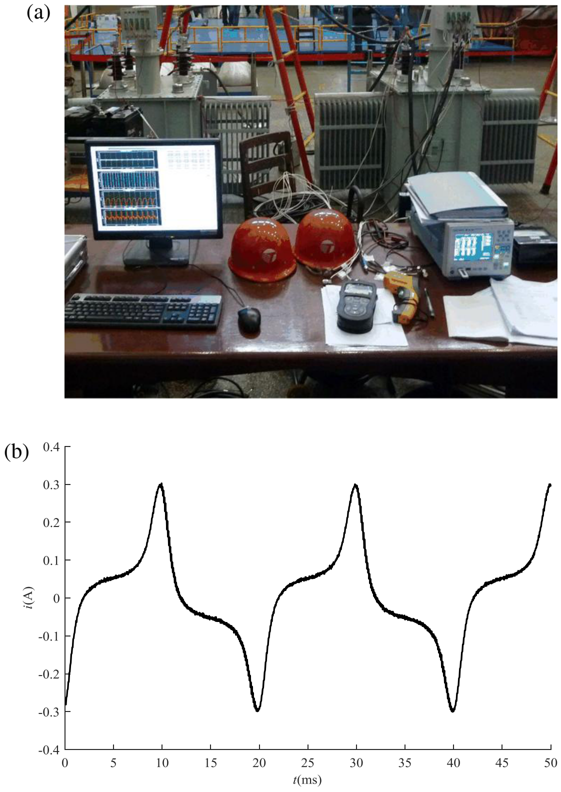

**FIGURE C4**. Experiment of the transformer. (a) Field experiment. (b) No-load current.

## REFERENCES

[1] Santos, R. R., M. A. Pais, J. M. R. Cardoso, J. A. Ribeiro, and F. J. G. Pinheiro, "The influence of Shield Wires on GIC simulations for realistic power grids," *Electric Power Systems Research*, Vol. 244, 111540, 2025.

[2] Rezaei-Zare, A., L. Marti, A. Narang, and A. Yan, "Analysis of three-phase transformer response due to GIC using an advanced duality-based model," *IEEE Transactions on Power Delivery*, Vol. 31, No. 5, 2342–2350, Oct. 2016.

[3] Mousavi, S. A. and D. Bonmann, "Analysis of asymmetric magnetization current and reactive power demand of power transformers due to GIC," *Procedia Engineering*, Vol. 202, 264–272, 2017.

[4] Fang, Z., Y. Shen, K. Gao, Y. Rao, C. Li, and Y. Rao, "Effect of GIC's frequency variation on transformer bias," in *2020 IEEE 4th Conference on Energy Internet and Energy System Integration (EI2)*, 1245–1250, Wuhan, China, 2020.

[5] Saleh, S. A., E. W. Zundel, G. Young-Morris, J. Meng, J. Cardenas, E. F. S. Hill, and S. Brown, "Impacts of transformer loading on the harmonic distortion created by GIC flows," *IEEE Transactions on Industry Applications*, Vol. 60, No. 3, 4666–4676, May-Jun. 2024.

[6] Akbari, M. and A. Rezaei-Zare, "Thermal analysis of power transformers under geomagnetically induced current," *IEEE Transactions on Power Delivery*, Vol. 38, No. 6, 4114–4121, Dec. 2023.

[7] Behdani, B., M. Tajdinian, M. Allahbakhshi, M. Popov, M. Shafie-khah, and J. P. S. Catalão, "Experimentally validated extended kalman filter approach for geomagnetically induced current measurement," *IEEE Transactions on Industrial Electronics*, Vol. 69, No. 6, 6316–6328, Jun. 2022.

[8] Rezaei-Zare, A., "Reactive power loss versus GIC characteristic of single-phase transformers," *IEEE Transactions on Power Delivery*, Vol. 30, No. 3, 1639–1640, Jun. 2015.

[9] Saleh, S. A., E. W. Zundel, D. Jewett, E. F. S. Hill, J. Meng, G. Y. Morris, and S. Brown, "Case studies of harmonic distortion in power transformers due to geomagnetically induced current flows," in *2023 IEEE/IAS 59th Industrial and Commercial Power Systems Technical Conference (I&CPS)*, 1–7, Las Vegas, NV, USA, 2023.

[10] Behjat, V., M. Mostafaei, A. Rezaei-Zare, and M. A. M. Cheema, "Analysis of power transformers under geomagnetically induced currents," in *2023 IEEE Kansas Power and Energy Conference (KPEC)*, 1–5, Manhattan, KS, USA, 2023.

[11] Li, Y.-C. and L.-G. Liu, "The application of the wavelet packet to the study of vibration of transformer under DC magnetic bias," in *2010 5th International Conference on Critical Infrastructure (CRIS)*, 1–4, Beijing, China, 2010.

[12] Pan, C., C. Wang, and H. Su, "Excitation current and vibration characteristics of DC biased transformer," *CSEE Journal of Power and Energy Systems*, Vol. 7, No. 3, 604–613, 2019.

[13] Zhu, L., Q. Yang, R. Yan, X. Zhang, and Y. Yang, "Research on dynamic vibration of transformer with wireless power transfer system load," *IEEE Transactions on Magnetics*, Vol. 51, No. 11, 1–4, Nov. 2015.

[14] Wang, Y., W. Zhen, Y. Bao, J. Zhang, H. Zhang, and J. Yang, "A unified magnetic equivalent circuit model for transformer core saturation analysis in multiphysics simulations," in *2024 The 9th International Conference on Power and Renewable Energy (ICPRE)*, 344–348, 2024.

[15] Duan, J., Y. Bao, G. Zhang, X. Wang, P. Jiang, W. Niu, H. Zhang, W. Zhen, Y. Xia, and R. Song, "Modeling and simulation analysis of three-phase saturable transformers: A study on the effects of geomagnetically induced current on transformers," *Energies*, Vol. 18, No. 4, 824, 2025.

[16] Diao, G., H. Ni, W. Si, Y. Gu, and J. Yang, "Multi-physics numerical research in oil-immersed three-phase transformer under load unbalance," *Energies*, Vol. 18, No. 5, 1217, 2025.

[17] Yuan, F., Z. Yan, R. Zhang, Y. Yang, S. Jian, and B. Tang, "Research on vibration characteristic analysis and fault diagnosis method of oil-immersed transformer based on multi-physics coupling," *IEEJ Transactions on Electrical and Electronic En-*

*gineering*, Vol. 19, No. 10, 1621–1630, 2024.

[18] Liu, C., X. Wang, C. Lin, and J. Song, "Proximity effects of lateral conductivity variations on geomagnetically induced electric fields," *IEEE Access*, Vol. 7, 6240–6248, 2018.

[19] He, J., Z. Yu, R. Zeng, and B. Zhang, "Vibration and audible noise characteristics of AC transformer caused by HVDC system under monopole operation," *IEEE Transactions on Power Delivery*, Vol. 27, No. 4, 1835–1842, Oct. 2012.

[20] Yorozu, T., M. Hirano, K. Oka, and Y. Tagawa, "Electron spectroscopy studies on magneto-optical media and plastic substrate interface," *IEEE Translation Journal on Magnetics in Japan*, Vol. 2, No. 8, 740–741, Aug. 1987.

[21] Liu, C.-M., L.-G. Liu, and R. Pirjola, "Geomagnetically induced currents in the high-voltage power grid in China," *IEEE Transactions on Power Delivery*, Vol. 24, No. 4, 2368–2374, Oct. 2009.

[22] Arabsalmanabadi, B., H. Arab, V. H. G. Amador, S. Dufour, and K. Al-Haddad, "A three-dimensional discontinuous Galerkin time-domain finite element method for electromagnetic modeling of wireless power transfer coils," *IEEE Open Journal of the Industrial Electronics Society*, Vol. 2, 360–371, 2021.

[23] Zhao, Y., W. Chen, M. Jin, T. Wen, J. Xue, Q. Zhang, and M. Chen, "Short-circuit electromagnetic force distribution characteristics in transformer winding transposition structures," *IEEE Transactions on Magnetics*, Vol. 56, No. 12, 1–8, Dec. 2020.

[24] Chao, P., X. Chen, and G. Cai, "Mode-state characteristics of three-phase unbalanced operation winding vibration of transformer based on electromagnetic mechanical coupling principle," *Proceedings of the CSEE*, Vol. 40, No. 14, 4695–4707, 2020.

[25] Song, W., Y. Han, F. Yang, J. Pang, L. Wang, J. Cao, and S. Deng, "Magnetostrictive vibration characteristics of amorphous alloy transformer with three-dimensional wound core," *IEEE Access*, Vol. 12, 43 958–43 967, 2024.

[26] Chen, Z., Q. Zhou, G. Ding, X. Wu, J. Wu, and Y. Zhang, "Influence of magnetic state variation on transformer core vibration characteristics and its measurement," *IEEE Transactions on Instrumentation and Measurement*, Vol. 71, 1–8, 2022.